Chin. Phys. Lett. **39**, 017501 (2022) **Express Letter**

The 20-nm Skyrmion Generated at Room Temperature by Spin-Orbit Torques

Jiahao Liu(刘嘉豪)[1,2,3†], Zidong Wang(王子东)[1,2†], Teng Xu(许腾)[1,2], Hengan Zhou(周恒安)[1,2], Le Zhao(赵乐)[1,2], Soong-Guen Je[4,5], Mi-Young Im[4], Liang Fang(方粮)[3], and Wanjun Jiang(江万军)[1,2*]

[1]*State Key Laboratory of Low-Dimensional Quantum Physics and Department of Physics, Tsinghua University, Beijing 100084, China*
[2]*Frontier Science Center for Quantum Information, Tsinghua University, Beijing 100084, China*
[3]*Institute for Quantum Information & State Key Laboratory of High Performance Computing, College of Computer, National University of Defense Technology, Changsha 410073, China*
[4]*Center for X-ray Optics, Lawrence Berkeley National Laboratory, Cyclotron Road, Berkeley, CA 94720, USA*
[5]*Department of Physics, Chonnam National University, Gwangju, 61186, Republic of Korea*

(Received 2 November 2021; accepted 3 December 2021; published online 13 December 2021)

The discovery of magnetic skyrmions provides a promising pathway for developing functional spintronic memory and logic devices. Towards the future high-density memory application, nanoscale skyrmions with miniaturized diameters, ideally down to 20 nm are required. Using x-ray magnetic circular dichroism transmission microscopy, nanoscale skyrmions are observed in the $[Pt/Co/Ir]_{15}$ multilayer at room temperature. In particular, small skyrmions with minimum diameters approaching 20 nm could be generated by the current-induced spin-orbit torques. Through implementing material specific parameters, the dynamic process of skyrmion generation is further investigated by performing micromagnetic simulations. According to the simulation results, we find that both the tube-like Néel-type skyrmions and the bobber-like Néel-type skyrmions can be electrically generated. In particular, the size of the bobber-like Néel-type skyrmions can be effectively reduced by the spin-orbit torques, which leads to the formation of 20 nm Néel-type skyrmions. Our findings could be important for understanding the formation dynamics of nanoscale Néel-type spin textures, skyrmions and bobber in particular, which could also be useful for promoting nanoscale skyrmionic memories and logic devices.

DOI: 10.1088/0256-307X/39/1/017501

Magnetic skyrmions are considered to be one of the ideal information carriers for spintronic devices due to the advantages of topological protection, and low energy consumption.[1−13] Since the original theoretical prediction,[14,15] Bloch-type skyrmions were firstly observed in B20-type non-centrosymmetric compounds (such as FeGe,[16] FeCoSi,[17] MnFeGe[18] and MnSi[19−26]), which however mainly exist at low temperature. Meanwhile, Néel-type skyrmions[27,28] stabilized by the interfacial Dzyaloshinskii–Moriya interaction (i-DMI) have been found in the heavy metal/ferromagnet (HM/FM) bilayer with an interfacial asymmetry, such as Pt/CoFe/MgO,[29,30] Pt/Co/Ni/Co/TaN[31] and Pt/Co/AlO_x.[32] Furthermore, a strong i-DMI have been identified in magnetic multilayers made of HM/FM bilayers, which leads to the formation of Néel-type skyrmions at room temperature.[33,34] For example, Néel-type skyrmions were stabilized in Ta/CoFeB/TaO_x, Pt/Co/Ta and Pt/CoFeB/MgO multilayers, together with their intriguing spin-torque-driven dynamics.[35−37] In particular, Néel-type skyrmions below 100 nm in diameter are observed at room temperature in Ir/Co/Pt multilayers,[38,39] Ta/Co/W multilayer,[40] Co/Pd multilayer,[41] Ir/Fe/Co/Pt multilayer,[42,43] Pt/Co/IrMn multilayer[44] and Pt/SmCo/Ta multilayer.[45] Note that ferrimagnetic skyrmions of diameter 10 nm have been observed in Pt/CoGd/Ta trilayer, which however suffers from a temperature sensitive magnetization,[46] limiting its future applications. By contrast, an experimental realization of room-temperature sub-50 nm in ferromagnetic films remains as a challenge. It should be emphasized here that since the size of skyrmion directly determines the cell size of the skyrmion-based racetrack memory,[47−51] the realization of sub 50 nm skyrmion could substantially improve the storage density of skyrmionic devices.[25,52]

In this work, we explore the formation of room-temperature nanoscale Néel-type skyrmions in a multilayer of $[Pt(1.5\,nm)/Co(1\,nm)/Ir(1.5\,nm)]_{15}$ using an x-ray magnetic circular dichroism (XMCD) transmission microscopy, which is made possible by utilizing the current-induced spin-orbit torques (SOTs). Following the increased current densities and hence the accompanied SOTs, sizes of Néel-type skyrmions decrease accordingly, with the smallest diameter approaching 20 nm. By performing a layer-resolution

†These authors contributed equally to this work.
*Corresponding author. Email: jiang_lab@tsinghua.edu.cn
© 2022 Chinese Physical Society and IOP Publishing Ltd

micromagnetic simulation, the formation process of Néel-type skyrmions can be captured. The revelation of three-dimensional spin textures, including bobber-like and tube-like skyrmions in the present material system could be useful for skyrmionics.

Materials and Methods—Sample Preparation and Measurement. The multilayer sample is grown by using ultrahigh vacuum magnetron sputtering at room temperature with the base pressure of the main chamber at 2×10^{-8} Torr. The sputtering is performed in an argon atmosphere of pressure 3 mTorr, and the sputtering rate is 0.02 nm/s for all layers. A 2 nm Ta on 100 nm Si_3N_4 is used as a seeding layer, which is followed by growing of 15 stacks of Pt(1.5 nm)/Co(1 nm)/Ir(1.5 nm), and finally a 2 nm Ta as a protective layer. The device is prepared using electron beam lithography and followed by a lift-off process. The magnetic hysteresis loop is obtained by using a vibrating sample magnetometer (VSM). The multilayer is also grown on 100 nm thickness Si_3N_4 membrane (Clean SiN, Suzhou) for the XMCD transmission microscopy imaging experiment. The XMCD imaging in transmission mode is carried out at the Co L_3 edge (778.5 eV) using a full-field soft x-ray transmission microscope (XM-1) at the beamline 6.1.2 at the Advanced Light Source of Lawrence Berkeley National Laboratory, with a spatial resolution better than 20 nm.[53] The nonmagnetic structural defect would not contribute to the magnetic contrast.

Micromagnetic Simulations. We simulate 15 magnetic layers with i-DMI and dipolar interaction using a micromagnetic simulation software Mumax3. The current-induced SOT is also added to the Landau–Lifshitz–Gilbert (LLG) equation. The relax-state solution of the system is calculated after each current pulse. The calculation unit size is $2 \times 2 \times 1\,\mathrm{nm}^3$, the saturation magnetization $M_s = 1200\,\mathrm{kA/m}$, the exchange constant $A = 10\,\mathrm{pJ/m}$, the damping coefficient $\alpha = 0.01$, the perpendicular magnetization anisotropy $K_u = 750\,\mathrm{kJ/m}^3$, the i-DMI intensity $D = 1.6\,\mathrm{mJ/m}^2$,[38] and the perpendicular magnetic field $H_z = 233\,\mathrm{mT}$.

Results—Room-Temperature Skyrmions in the Pt/Co/Ir Multilayer. The Pt/Co/Ir trilayer is known for hosting a very large strength of i-DMI which could be advantageous for stabilizing nanoscale Néel-type skyrmions.[38] This fact motivates us to explore the miniaturized size of skyrmions in this material system. In order to study the current-induced nanoscale Néel-type skyrmions, a magnetic multilayer of composition and stacking order $[\mathrm{Pt}(1.5\,\mathrm{nm})/\mathrm{Co}(1\,\mathrm{nm})/\mathrm{Ir}(1.5\,\mathrm{nm})]_{15}$ is synthesized, as schematically shown in Fig. 1(a). The out-of-plane magnetic hysteresis loop (M–H_z) is measured by using VSM, as shown in Fig. 1(b). The shape of the loop is similar to the typical multilayers that host Néel-type skyrmions.[35,42–45] The saturation magnetization is estimated to be $M_s = 1200\,\mathrm{kA/m}$.

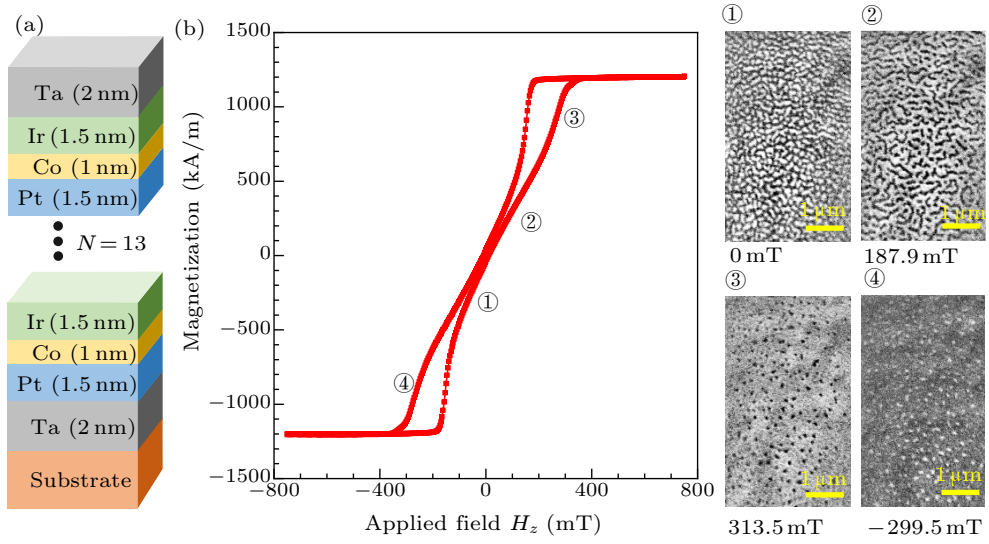

Fig. 1. Magnetic properties of the Pt/Co/Ir multilayer. (a) Schematic illustration of the $[\mathrm{Pt/Co/Ir}]_{15}$ multilayer film. A 2-nm-thick Ta layer is sputtered on the substrate as a seeding layer and another 2-nm-thick Ta layer on the top is used as a protective layer. (b) The perpendicular magnetic hysteresis loop (M–H_z) of the multilayer. The magnetic domain configurations at the selected magnetic fields (H_z) were recorded by using an XMCD transmission microscope. Room-temperature skyrmions are observed at $\sim\pm300$ mT. The scale bar is 1 μm.

The XMCD images collected at the Co L_3 edge under perpendicular fields (H_z) are given on the right of Fig. 1. The black color corresponds to the local magnetization pointing downward ($m_z < 0$) and the white color corresponds to the local magnetization pointing upward ($m_z > 0$). The evolution of magnetic domain configurations as a function of H_z can be found in Fig. S1 of the Supplementary Materials. Initially, the size of the skyrmions decreases with the increased amplitude of H_z. When $H_z > 299$ mT, the average diameter of skyrmions remains as a constant at approximately 58 nm. The pinning effect from structural

defect that typically exists in Co-based magnetic multilayer could be responsible for the fixed diameter.[40]

The 20-nm Skyrmion Induced by Current Pulses. In order to probe the dynamics of skyrmion driven by the current-induced SOTs, we apply current pulses with different durations and amplitudes to the microstripe device made of multilayer. An optical image of the device is shown in Fig. 2(a). Current pulses are applied to the multilayer through the Ta/Pt electrodes on both sides, where the white arrow indicates the positive direction of the current flow. Due to the involvement of heavy metal and the resulting conversion from the charge current to spin current, the current-induced SOTs are expected in the multilayers.[54,55] Before applying pulse (at $H_z = 233\,\mathrm{mT}$), the multilayer is at a coexisting stripe domain-skyrmion state. After applying current pulses of a fixed duration 50 µs with increased current densities (from $0.6\times10^{10}\,\mathrm{A/m^2}$ to $2.4\times10^{10}\,\mathrm{A/m^2}$), the pristine stripe domains are dissected (at $0.6\times10^{10}\,\mathrm{A/m^2}$), then a densely packed skyrmion phase is formed (at $1.6\times10^{10}\,\mathrm{A/m^2}$). Following the increased amplitudes (from $1.6\times10^{10}\,\mathrm{A/m^2}$ to $2.4\times10^{10}\,\mathrm{A/m^2}$), the number of skyrmions decreases accordingly, which can be seen in Fig. S2 of the Supplementary Materials.

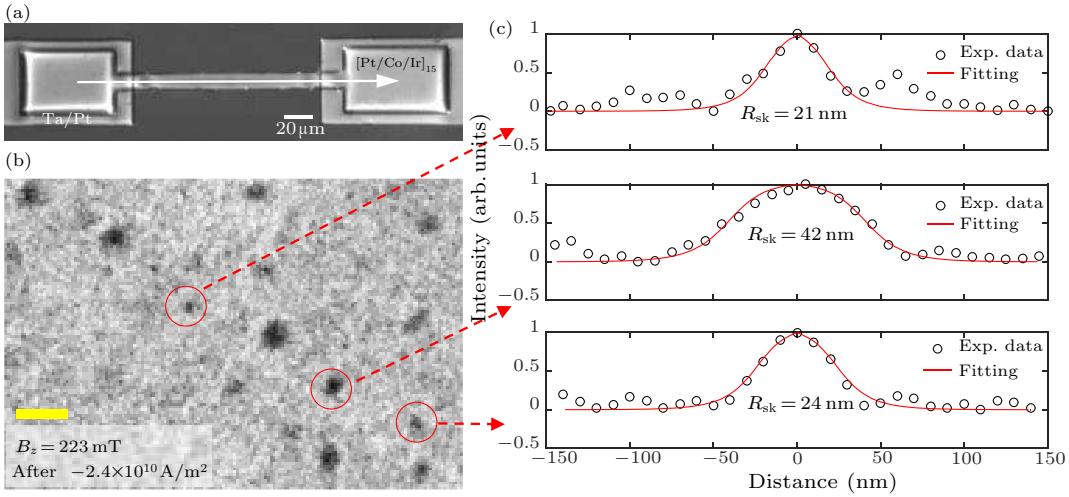

Fig. 2. The generation of nanoscale skyrmions by current pulse at room temperature. (a) An optical image of the device. The white arrow indicates the direction of the current pulse. The scale bar is 20 µm. (b) The XMCD images taken after applying a current pulse of amplitude $-2.4\times10^{10}\,\mathrm{A/m^2}$ and of duration 50 µs, at $H_z = -223\,\mathrm{mT}$. The scale bar is 200 nm. (c) The profile of the three selected skyrmions marked by red circles. The black circles are the experimental data extracted from the XCMD images, and the red line is the fitted profile. The estimated diameters of the three skyrmions are 21 nm, 42 nm, and 24 nm, respectively.

Negative pulses are subsequently applied to reveal the evolution of skyrmion sizes as a function of pulse currents. Figure 2(a) shows an exemplary XMCD image taken after applying a pulse of amplitude $-2.4\times10^{10}\,\mathrm{A/m^2}$. From this image data, one can clearly observe the generation of nanoscale skyrmions by the current-induced SOTs. In order to precisely determine the size of skyrmions, we utilize a 360° domain wall model in which the polar angle $\Theta_0(r)$ of the spin rotation, describing the static profile of the Néel-type skyrmion, satisfies the equilibrium equation obtained by minimizing the energy functional:[56]

$$\nabla^2\Theta_0 = \left[\xi^2 + \frac{1}{r^2}\right]\sin\Theta_0\cos\Theta_0 - \frac{d}{r}\sin^2\Theta_0 + h\sin\Theta_0, \tag{1}$$

where $\xi^2 = 2K_\mathrm{u}/\mu_0 M_\mathrm{s}^2 - 1$, $h = H_z/M_\mathrm{s}$, $r = \rho/l_\mathrm{ex}$ is the reduced polar coordinate and $d = |D|\,l_\mathrm{ex}/A$. The exchange length $l_\mathrm{ex} = \sqrt{2A}/\mu_0 M_\mathrm{s}^2$. M_s is the saturation magnetization, μ_0 is the vacuum permeability, A is the exchange constant, K_u is the magnetization anisotropy constant, D is the i-DMI strength, and H_z is the applied magnetic field. An approximate lowest energy solution in the form of $\tan[\Theta_0(r)/2] = r_\mathrm{sk}/r\cdot e^{\xi(r_\mathrm{sk}-r)}$ is used to fit the skyrmion profile.[56] The fitting results are shown in Fig. 2(b). The diameters of the three representative skyrmions are clearly identified by the full width at half maximum (FWHM) of the fitting line profile as 21 nm, 42 nm, and 24 nm, respectively.

Subsequently, we investigate the size distribution of skyrmions under the increased amplitudes of pulse currents. As indicated in Fig. 3(a), a gray value threshold is employed to identify the skyrmions in the XMCD images, which are marked in red. The evolution of the estimated skyrmion diameters as a function of the increased current densities is shown in Fig. 3(b). As the current density increases, the average skyrmion diameter decreases from 42.5 nm down to 36.5 nm. The distribution of the skyrmion diameters as a function of the current density (from $0.6\times10^{10}\,\mathrm{A/m^2}$ to $2.4\times10^{10}\,\mathrm{A/m^2}$) is shown in Fig. 3(c).

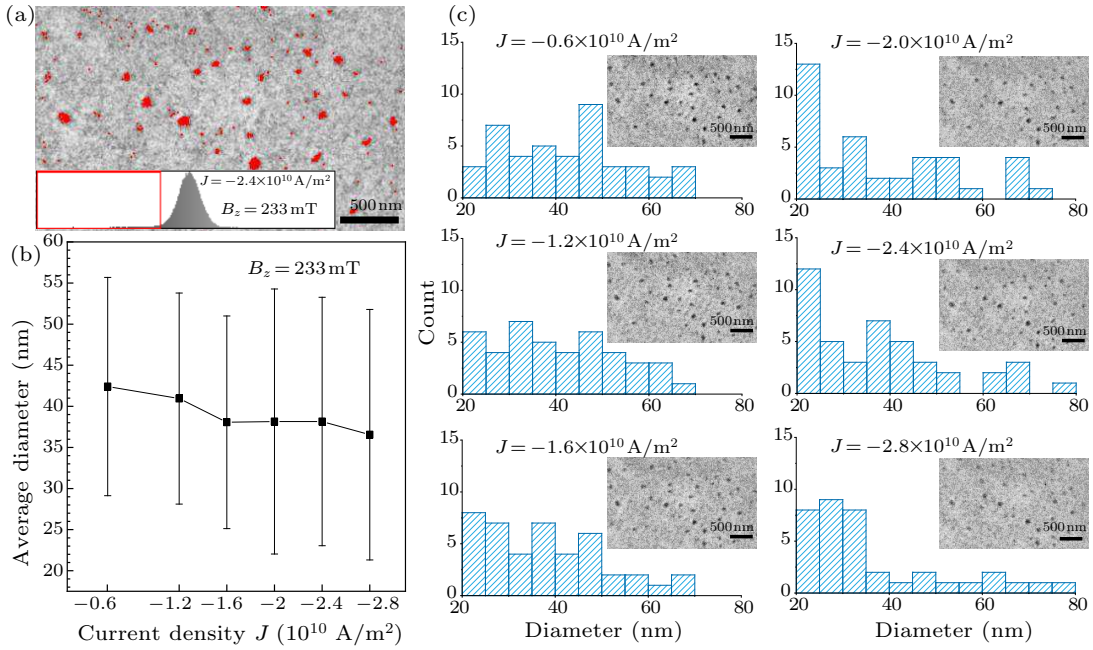

Fig. 3. The size distribution of skyrmions under pulses with various current densities. (a) A gray threshold method is used to identify skyrmions (marked in red). The scale bar is 500 nm. (b) The average diameter of skyrmions as a function of the current density. (c) The statistics of the skyrmion diameters under pulses with various current densities. The scale bar is 500 nm.

For most of skyrmions, the average diameters decrease with the increased current densities. However, we find that the sizes of few skyrmions remain unchanged. Shown in Fig. 4(a) is an example, which is from a selected area of Fig. 3(c). As the current density increases, one skyrmion on the upper-left corner shrinks in size (marked in yellow circle), while the sizes of the other two skyrmions on the right remain the same.

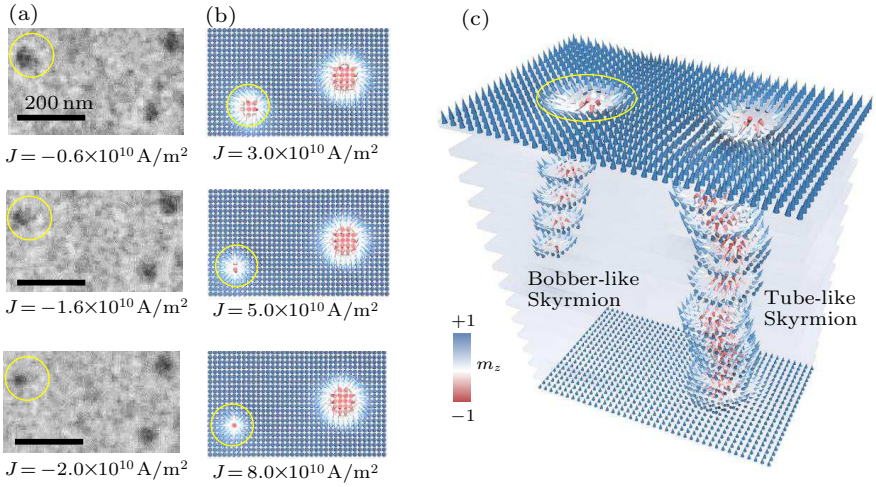

Fig. 4. Micromagnetic simulation of the response of skyrmion driven by the current-induced SOTs. (a) A selected area with three skyrmions from the XMCD images in Fig. 3(c) under the increased amplitude of the current pulse. The skyrmion marked by the yellow circle on the upper-left corner shrinks its size. The sizes of rest two skyrmions on the right, remain nearly the same. The scale bar is 200 nm. (b) The corresponding micromagnetic simulation under the increased current density, which is consistent with our experimental observations. The color from blue to red indicates m_z from 1 to −1 (upward to downward) while the cones represent the in-plane magnetization direction. (c) Three-dimensional view of the two types of skyrmions, which reveals the spin structures of a bobber-like skyrmion (left) and a tube-like skyrmion (right) in the present multilayer.

Discussion and Conclusion. Through applying electrical currents into the microstripe, the role of current-induced Joule heating, Oersted field and current-induced SOTs will be discussed. Regarding the Joule hearing, early studies demonstrated that distribution of skyrmions can be largely influenced, but not the size.[57] Through calculating the local temperature change, we also find that the value is smaller than the threshold temperature required to thermally generate skyrmions in similar systems.[53] The strength of Oersted field can be calculated by using a finite element method, as shown in Fig. S3. The out-of-plane component of Oersted field is opposite on the upper and lower sides of the multilayer. If the Oersted field plays a major role, the size of the skyrmions should be larger on one side and smaller on the other, which is absent from our data. With respect to the contribution from the current-induced SOTs, the underlying physics can be captured by performing the layer-resolved micromagnetic simulations, which is carried out by using the LLG equation[58] with the SOT terms:[59]

$$\dot{\boldsymbol{m}} = -\gamma \boldsymbol{m} \times [\boldsymbol{H}_{\text{eff}} + \tau_{\text{dam}}(\boldsymbol{m} \times \boldsymbol{p}) + \tau_{\text{fie}}\boldsymbol{p}] + \alpha \dot{\boldsymbol{m}} \times \boldsymbol{m}, \tag{2}$$

where γ is the gyromagnetic ratio, α is the damping coefficient, $\boldsymbol{m}$ is the normalized magnetization vector, $\dot{\boldsymbol{m}}$ is the time derivative of $\boldsymbol{m}$. $\boldsymbol{H}_{\text{eff}} = -\frac{1}{\mu_0 M_{\text{s}}}\frac{dE}{d\boldsymbol{m}}$ is the effective field where the energy E is given by $E = E_{\text{DMI}} + E_{\text{exch}} + E_{\text{demag}} + E_{\text{aniso}} + E_{\text{Zee}}$. Here τ_{dam} and τ_{fie} are amplitudes of the damping-like torque and field-like torque, respectively. In the typical SOT experiment, a damping-like torque $\tau_{\text{dam}} = \frac{\hbar\theta_{\text{SH}}J_{\text{c}}}{2e\mu_0 M_{\text{s}} d}$ plays a major role, where $\hbar$ is the reduced Planck constant, θ_{SH} is the spin Hall angle, J_{c} is the current density flowing in the heavy metal layer, e is the elementary charge, μ_0 is vacuum permeability, and d is the thickness of the ferromagnetic layer. For a heavy metal/ferromagnet bilayer, the current pulse is applied in the $\hat{x}$ direction, the spin polarization vector is given by $\boldsymbol{p} = \text{sign}(\theta_{\text{SH}})\hat{j} \times \hat{n} = -\hat{y}$ (surface normal $\hat{n} = \hat{z}$).

We consider the Neumann boundary conditions, and the i-DMI energy is given by[60]

$$E_{\text{DMI}} = D[m_z(\nabla \cdot \boldsymbol{m}) - (\boldsymbol{m} \cdot \nabla)m_z], \tag{3}$$

where D is the i-DMI strength. The i-DMI contribution can be obtained by

$$\boldsymbol{H}_{\text{DMI}} = -\frac{1}{\mu_0 M_{\text{s}}}\frac{dE_{\text{DMI}}}{d\boldsymbol{m}} = -\frac{2D}{\mu_0 M_{\text{s}}}[(\nabla \cdot \boldsymbol{m})\hat{z} - \nabla m_z]. \tag{4}$$

Due to the strong i-DMI in the $[\text{Pt/Co/Ir}]_{15}$ multilayer, compact skyrmions in each layer exhibit the same Néel-type chirality, as can be seen from Figs. 4(b) and 4(c).

In the layer-resolved micromagnetic simulation, a mixture of stripe domain and isolated skyrmion is revealed at 223 mT. Figure 4(b) shows the simulation results of two individual Néel-type skyrmions from a selected area. The color from blue to red indicates the change of the $\hat{z}$-component of magnetization (m_z) from 1 to -1 (upward to downward), while cones represent the magnetization direction. It is found that the skyrmion on the left (marked in yellow circle) gradually shrinks in size, following an increased current density. The size and shape of the other skyrmion, however, remains the same. These simulation results are consistent with our experimental observations shown in Fig. 4(a).

Experimentally, the 15 magnetic layers are coupled through the interlayer dipolar interaction. In competition with the i-DMI,[61] the system may host two different types of skyrmions (hybridized and compact skyrmions), as shown in Fig. 4(c). One is the compact skyrmions existing across all magnetic layers and thus form tube-like skyrmions [the right skyrmion in Fig. 4(c)]. The other is the skyrmions that only exist in part of the magnetic layers [left skyrmion in Fig. 4(c)]. Note that this type of spin texture is similar to chiral bobber, which was experimentally observed in B20-type alloys[62] and Cu_2OSeO_3.[63] A chiral bobber is composed of a Bloch-point singularity and a skyrmion tube,[62,64,65] which can be useful for enabling reliable skyrmionic device at room temperature racetrack memory. Unlike Bloch-type bobber, the left skyrmion in Fig. 4(c) is discontinuous and does not have a Bloch point. In the following, we use the term bobber-like skyrmion to refer to this type of spin textures shown in Fig. 4(c). Note that the Néel-type bobber in multilayer stabilized by i-DMI is not reported yet. Through performing micromagnetic simulations, the competition between interlayer dipole coupling and iDMI in stabilizing bobber-like skyrmion in multilayer is revealed (see details in Figs. S4 and S5 of the Supplementary Materials).

A bobber-like skyrmion refers to different sizes of layer-dependent skyrmions across the multilayer, where sizes of skyrmions in the bottom layers are smaller than at the upper layer. Namely, the shape, size and position of skyrmion may vary from layer to layer. As a consequence, the shifted cores of skyrmions in different layers may subject to different strength of damping-like torques $\tau_{\text{dam}} m_z \hat{x}$. Following the migration of the upper and lower skyrmions, the $\hat{z}$-component of the local interlayer coupling $\boldsymbol{H}_{\text{dipole_}z} = \frac{2M_{\text{s}}}{4\pi R^3} m_{\text{i_}z}\hat{z}$ (R is the layer-to-layer distance and m_i is the normalized magnetic moment of the adjacent upper layer) is thus decreased. As a result, the bobber-like skyrmion is less bounded by the interlayer dipole coupling (see details in Fig. S6 of the Supplementary Materials), in comparison with the tube-like skyrmions, which gradually shrinks in size upon the applying the current-induced SOTs.

In conclusion, by using XMCD transmission imaging, we have experimentally observed the generation of room-temperature magnetic skyrmions with an av-

erage diameter of 58 nm in the Pt/Co/Ir multilayer. Skyrmions with the minimum diameter of ∼20 nm are further obtained by applying current pulses. Through performing a layer-resolved micromagnetic simulation, we have revealed that both bobber- and tube-like Néel-type skyrmions may coexist in the present multilayer. In particular, the bobber-like skyrmions are susceptible to the current-induced SOT, which shrink in size upon applying the current-induced SOTs. Our work could provide a meaningful route for generating nanoscale skyrmions at room temperature, which could be important for revealing the intriguing topological physics, and the compact skyrmion-based racetrack memory.

Acknowledgments. This work was supported by the Basic Science Center Project of NSFC (Grant No. 51788104), the National Key R&D Program of China (Grant No. 2017YFA020620), the Beijing Natural Science Foundation (Grant No. Z190009), the National Key R&D Program of China (Grant No. 2018YFB1003304), the National Natural Science Foundation of China (Grant Nos. 11774194, 51831005, 11861131008, 11804182, and 61832007), the Tsinghua University Initiative Scientific Research Program and the Beijing Advanced Innovation Center for Future Chip (ICFC). Works at the ALS were supported by U.S. Department of Energy (DE-AC02-05CH11231) and by Lawrence Berkeley National Laboratory through the Laboratory Directed Research and Development (LDRD) Program.

References

[1] Bogdanov A and Hubert A 1994 *J. Magn. Magn. Mater.* **138** 255
[2] Bogdanov A N and Rößler U K 2001 *Phys. Rev. Lett.* **87** 037203
[3] Fert A, Reyren N and Cros V 2017 *Nat. Rev. Mater.* **2** 17031
[4] Zang J *et al.* 2011 *Phys. Rev. Lett.* **107** 136804
[5] Nagaosa N and Tokura Y 2013 *Nat. Nanotechnol.* **8** 899
[6] Koshibae W *et al.* 2015 *Jpn. J. Appl. Phys.* **54** 053001
[7] Chen G *et al.* 2015 *Appl. Phys. Lett.* **106** 242404
[8] Braun H B 2012 *Adv. Phys.* **61** 1
[9] Buettner F *et al.* 2015 *Nat. Phys.* **11** 225
[10] Yang S H *et al.* 2021 *Nat. Rev. Phys.* **3** 328
[11] Gobel B, Mertig I and Tretiakov O A 2021 *Phys. Rep* **895** 1
[12] Back C *et al.* 2020 *J. Phys. D* **53** 363001
[13] Everschor-Sitte K *et al.* 2018 *J. Appl. Phys.* **124** 240901
[14] Skyrme T H R 1961 *Proc. R. Soc. A* **262** 237
[15] Bogdanov N Y and Yablonskii D A 1989 *Sov. Phys. JETP* **68** 101
[16] Huang S X and Chien C L 2012 *Phys. Rev. Lett.* **108** 267201
[17] Yu X Z *et al.* 2010 *Nature* **465** 901
[18] Shibata K *et al.* 2013 *Nat. Nanotechnol.* **8** 723
[19] Ritz R *et al.* 2013 *Nature* **497** 231
[20] Neubauer A *et al.* 2009 *Phys. Rev. Lett.* **102** 186602
[21] Pappas C *et al.* 2009 *Phys. Rev. Lett.* **102** 197202
[22] Tonomura A *et al.* 2012 *Nano Lett.* **12** 1673
[23] Yu X Z *et al.* 2013 *Nano Lett.* **13** 3755
[24] Du H F *et al.* 2014 *Nano Lett.* **14** 2026
[25] Jonietz F *et al.* 2010 *Science* **330** 1648
[26] Kindervater J *et al.* 2019 *Phys. Rev. X* **9** 041059
[27] Heinze S *et al.* 2011 *Nat. Phys.* **7** 713
[28] Romming N *et al.* 2013 *Science* **341** 636
[29] Emori S *et al.* 2013 *Nat. Mater.* **12** 611
[30] Boulle O *et al.* 2016 *Nat. Nanotechnol.* **11** 449
[31] DeRosa M C *et al.* 2010 *Nat. Nanotechnol.* **5** 91
[32] Pizzini S *et al.* 2014 *Phys. Rev. Lett.* **113** 047203
[33] Jiang W *et al.* 2017 *Phys. Rep.* **704** 1
[34] Dupe B *et al.* 2016 *Nat. Commun.* **7** 11779
[35] Woo S *et al.* 2016 *Nat. Mater.* **15** 501
[36] Jiang W *et al.* 2015 *Science* **349** 283
[37] Li W *et al.* 2019 *Adv. Mater.* **31** 1807683
[38] Moreau-Luchaire C *et al.* 2016 *Nat. Nanotechnol.* **11** 444
[39] Legrand W *et al.* 2017 *Nano Lett.* **17** 2703
[40] Jiang W *et al.* 2019 *Phys. Rev. B* **99** 104402
[41] Pollard S D *et al.* 2017 *Nat. Commun.* **8** 14761
[42] Soumyanarayanan A *et al.* 2017 *Nat. Mater.* **16** 898
[43] Raju M *et al.* 2019 *Nat. Commun.* **10** 696
[44] Guang Y *et al.* 2020 *Nat. Commun.* **11** 949
[45] Zhou H A *et al.* 2021 *Adv. Funct. Mater.* **31** 2104426
[46] Caretta L *et al.* 2018 *Nat. Nanotechnol.* **13** 1154
[47] Fert A, Cros V and Sampaio J 2013 *Nat. Nanotechnol.* **8** 152
[48] Parkin S S P, Hayashi M and Thomas L 2008 *Science* **320** 190
[49] Iwasaki J, Mochizuki M and Nagaosa N 2013 *Nat. Nanotechnol.* **8** 742
[50] Sampaio J *et al.* 2013 *Nat. Nanotechnol.* **8** 839
[51] Ding J J, Yang X F and Zhu T 2015 *J. Phys. D* **48** 115004
[52] Schulz T *et al.* 2012 *Nat. Phys.* **8** 301
[53] Wang Z *et al.* 2020 *Nat. Electron.* **3** 672
[54] Sinova J *et al.* 2015 *Rev. Mod. Phys.* **87** 1213
[55] Yu G Q *et al.* 2016 *Nano Lett.* **16** 1981
[56] Tomasello R *et al.* 2018 *Phys. Rev. B* **97** 060402(R)
[57] Lemesh I *et al.* 2018 *Adv. Mater.* **30** 1805461
[58] Landau L D and Lifshitz E M 1935 *Phys. Z. Sowjetunion* **8** 153
[59] Buttner F *et al.* 2017 *Nat. Nanotechnol.* **12** 1040
[60] Rohart S and Thiaville A 2013 *Phys. Rev. B* **88** 184422
[61] Bernand-Mantel A *et al.* 2020 *Phys. Rev. B* **101** 045416
[62] Zheng F *et al.* 2018 *Nat. Nanotechnol.* **13** 451
[63] Ran K *et al.* 2021 *Phys. Rev. Lett.* **126** 017204
[64] Zhu J *et al.* 2021 *Sci. Chin. Phys. Mech. Astron.* **64** 227511
[65] Gong Z Z *et al.* 2021 *Phys. Rev. B* **104** L100412

Supplementary Materials for **"The 20-nm Skyrmion Generated at Room Temperature by Spin-Orbit Torques"**

Jiahao Liu(刘嘉豪)[1,2,3,⊥] , Zidong Wang(王子东)[1,2,⊥], Teng Xu(许腾)[1,2], Hengan Zhou(周恒安)[1,2], Le Zhao(赵乐)[1,2], Soong-Guen Je[4,5], Mi-Young Im[4], Liang Fang(方粮)[3], Wanjun Jiang(江万军)[1,2,**]

[1]State Key Laboratory of Low-Dimensional Quantum Physics and Department of Physics, Tsinghua University, Beijing 100084, China

[2]Frontier Science Center for Quantum Information, Tsinghua University, Beijing 100084, China

[3]Institute for Quantum Information & State Key Laboratory of High Performance Computing, College of Computer, National University of Defense Technology, Changsha 410073, China

[4]Center for X-ray Optics, Lawrence Berkeley National Laboratory, Cyclotron Road, Berkeley, CA 94720, USA

[5]Department of Physics, Chonnam National University, Gwangju, 61186, Republic of Korea

[⊥]These authors contributed equally to this work.

[**]Corresponding author: Wanjun Jiang, email: jiang_lab@tsinghua.edu.cn, tel: 010-62793680, fax: 010-62781604.

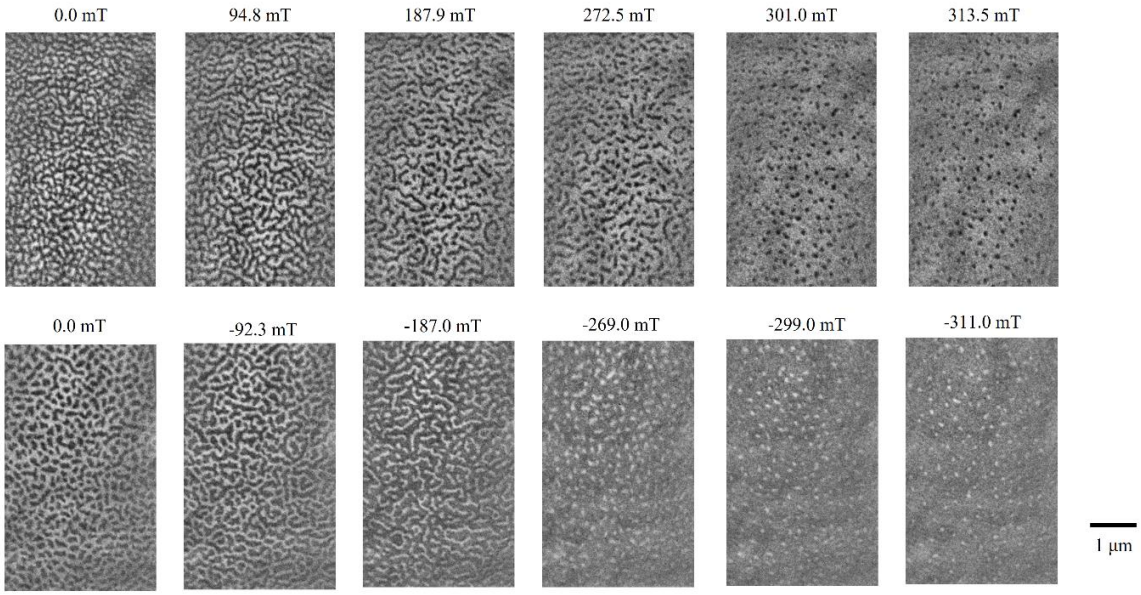

Figure S1. The XMCD images of magnetic domains under positive or negative perpendicular magnetic fields. The scale bar is 1 μm. As the magnetic field increases, the magnetic domain configurations change from stripe domains to isolated skyrmions. When the magnetic field continues to increase, the number of skyrmions decreases. However, when the magnetic field is increased above 299 mT, the average diameter of skyrmions remains about 58 nm and does not change following the increase of magnetic field. Since the maximum magnetic field of XM-1 is limited to 313.5 mT, we cannot further increase the perpendicular magnetic field until its full saturation.

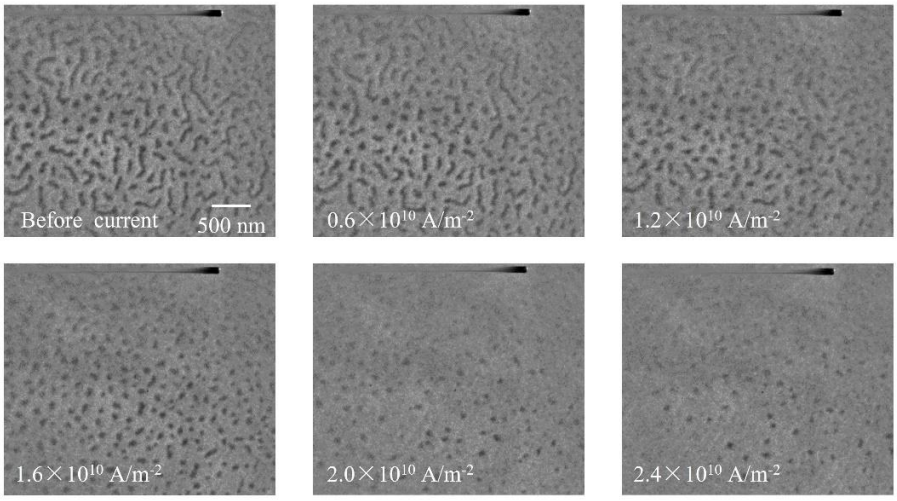

Figure S2. The XMCD images of magnetic domain configurations under pulse currents with various amplitudes. The scale bar is 500 nm. As the current density increases, the magnetic domain configurations change from stripe domains to densely packed skyrmions. When the amplitude of the current pulse continues to increase, the number of skyrmions decreases. The measurements are carried out under H_z = 223 mT.

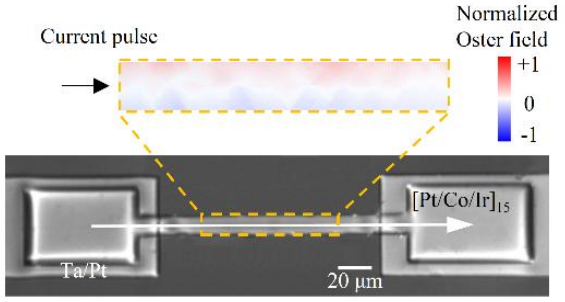

Figure S3. Finite element simulations of the out-of-plane component of Oersted field by using COMSOL software. The out-of-plane component of Oersted field is opposite on the upper and lower sides of the multilayer.

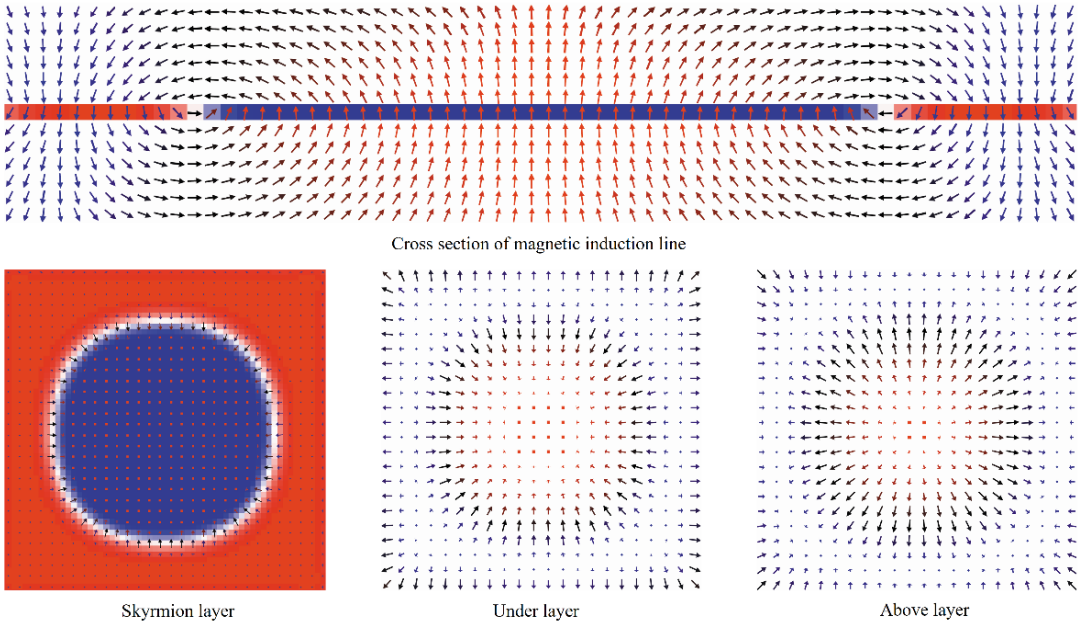

Figure S4. Micromagnetic simulation on the magnetic induction lines of a single layer of skyrmion. Above and below the skyrmion layer, the magnetic induction lines show completely opposite chirality. Extending the results to a multilayer system with i-DMI, the interlayer coupling produces two opposite chiralities that are existing at the top and bottom magnetic layers in the multilayers. Competition between iDMI and interlayer coupling in different multilayer systems results in uneven distribution of skyrmions in interlayer systems. In multilayers with small iDMI, for example in $[Ta/CoFeB/MgO]_{15}$[1], skyrmion transitions from Néel layers through a Bloch layer to the opposite chiral Néel layers.

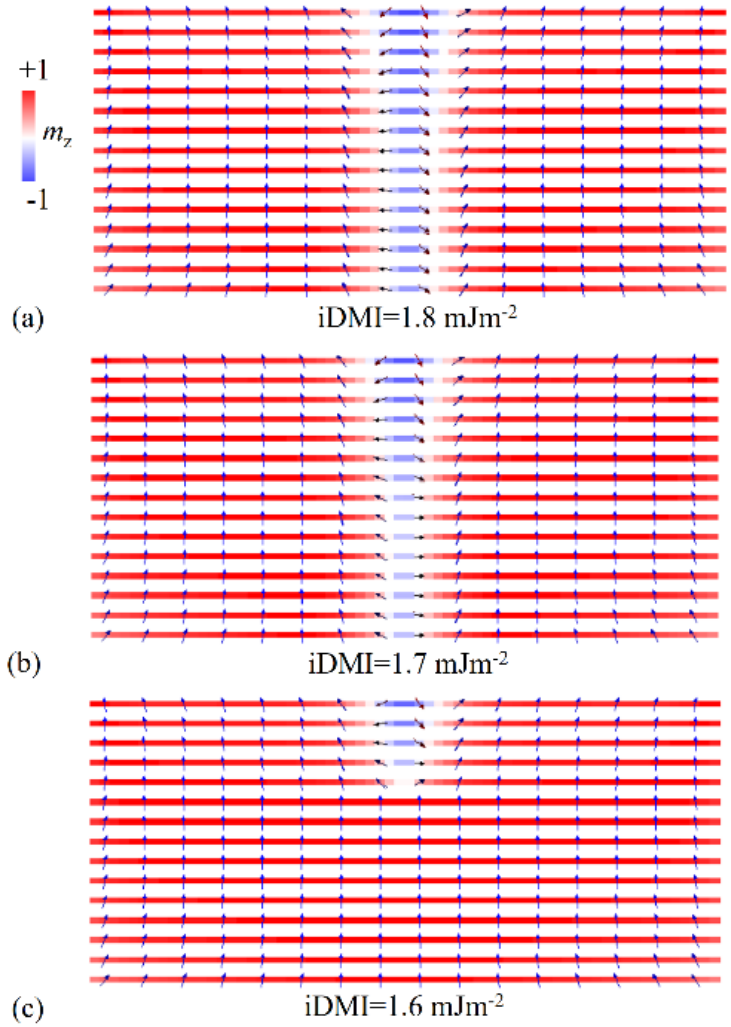

Figure S5. Micromagnetic simulations of skyrmion in multilayers with large iDMI. (a) When iDMI is large enough (1.8 mJm^{-2}), a tube-like Néel skyrmion is formed in the multilayer. (b) When iDMI becomes smaller (1.7 mJm^{-2}), the diameter of skyrmion tube is big at the top magnetic layer and small at the bottom magnetic layer. This is due to the competition between the interlayer coupling and iDMI. (c) With the further decrease of iDMI (1.6 mJm^{-2}), the skyrmion at lower layers disappear. The calculation unit size is 2 × 2 ×1 nm^3, the saturation magnetization M_s = 1200 kA/m, the exchange constant A = 10 pJm^{-1}, the damping coefficient α = 0.01, the perpendicular magnetization anisotropy K_u = 750 kJm^{-3}, and the external magnetic field H_z = 233 mT.

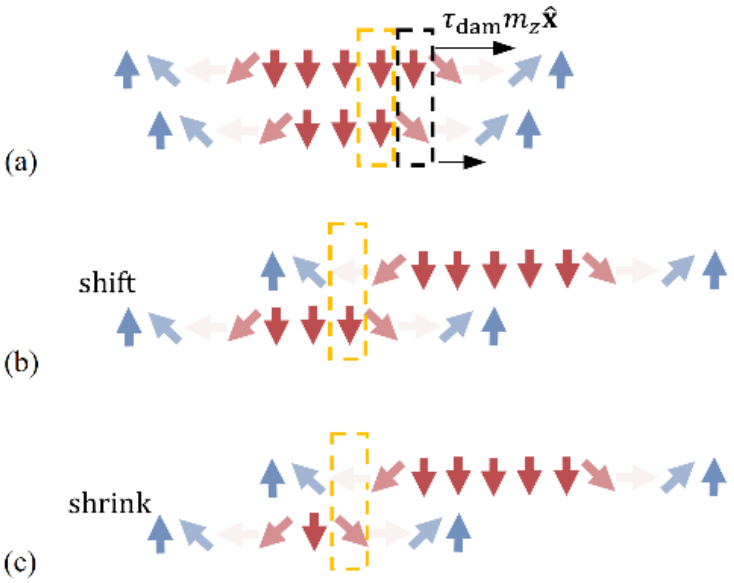

Figure S6. Bobber like-skyrmion under SOT. A bobber-like skyrmion exhibits a layer dependent magnetism across the magnetic multilayer. Namely, the size, shape and position of skyrmions in each layer could be very different. For example, the size of skyrmions at the bottom layers are smaller than that of the upper layers. (a) Therefore, skyrmions in different layers are subjected to different strength of damping-like torques $\tau_{\mathrm{dam}} m_z \hat{\mathbf{x}}$. (b) As a consequence, the cores of the skyrmions in the adjacent layers could be shifted. The local field of the interlayer dipole coupling is mainly generated by the adjacent layers, as $\mathbf{H}_{\mathrm{dipole_}z} = \frac{2M_s}{4\pi R^3} m_{i_z} \hat{\mathbf{z}}$, where R is the layer-to-layer distance and m_i is the normalized magnetic moment of the adjacent layers. (c) Following the migration of the upper and lower skyrmions, it can be seen from the magnetic moments marked in the orange box that the $\hat{\mathbf{z}}$-component of the interlayer coupling becomes smaller. This eventually leads to the shrinking of the size of skyrmion in the bottom magnetic layer.

Reference

[1] W. Li, I. Bykova, S. Zhang, G. Yu, R. Tomasello, M. Carpentieri, Y. Liu, Y. Guang, J. Grafe, M. Weigand, D. M. Burn, G. van der Laan, T. Hesjedal, Z. Yan, J. Feng, C. Wan, J. Wei, X. Wang, X. Zhang, H. Xu, C. Guo, H. Wei, G. Finocchio, X. Han, G. Schutz, *Adv Mater* **2019**, 31, e1807683.